Parallel-Path Power Flows in Magnetic-Geared Permanent Magnet Machines with Sandwiched Armature Stator

Yujun Shi[1,2], *Jin Wei*[1,2], *and Linni Jian*[1,2]*

(1. Department of Electrical and Electronic Engineering, Southern University of Science and Technology, Shenzhen, 518055, China;
2. Shenzhen Key Laboratory of Electric Direct Drive Technology, Shenzhen, 518055, China)

Abstract: Due to the large torque density of magnetic gears(MGs), magnetic-geared permanent magnet machines(MGPMs) have become promising competitors in the family of direct-drive machines. According to the deployment of armature stators, MGPMs can be generally classified into three types, viz., MGPM with inner armature stator(MGPM-IAS), MGPM with outer armature stator(MGPM-OAS), and MGPM with sandwiched armature stator(MGPM-SAS). Our investigation finds out that the MGPM-SAS can achieve parallel-path power flows better than the MGPM-OAS, while the MGPM-IAS is with serial power flow paths. Therefore, the torque capability of MGPM-IAS is limited by the torque transmission capability of its integrated MG. However, the MGPM-SAS has the possibility to offer even higher output torque than its integrated MG. This paper focuses on the MGPM-SAS. And three typical MGPMs and their power flow paths are introduced; the interaction of electromagnetic fields in MGPM-SAS is analyzed; simulation calculation and experimental verification are conducted to demonstrate the validity of the theoretical analysis.

Keywords: Direct drive, permanent magnet, magnetic gear, integrated machines, flux modulation, power flows.

1 Introduction

Magnetic gears(MGs) working on the field modulation effect have been proposed for more than a decade[1]. Due to the unique coaxial topology involved, the utilization of permanent magnet (PM) materials is greatly improved[2], which allows these MGs the capability of offering satisfactorily high torque density when achieving non-contact torque transmission and speed variation[3]. Compared with mechanical gears, MGs are able to eliminate the nuisance arising from the contact metal teeth, such as need of regular lubrication and maintenance, risks of fatigue failures, friction losses and so forth. Moreover, they can achieve physical isolation between the two mechanical power ports, and offer self-protection in case of overload. Therefore, MGs have enormous potential to be widely used in all kinds of applications.

Great progress has been made in design and application of MGs most recently. Halbach PM arrays are adopted to suppress the torque ripple of MGs[4]. Flux-focusing magnets can improve the torque capability of MGs[5]. Linear MG is prototyped for aerospace application[6]. Axial flux MG using skew effect is investigated to mitigate the cogging torques[7].Shape of the modulating segments is optimized to improve the modulation effect[8]. The torque density of MGs can reach 100kN·m/m^3 or above, which is much higher than that of traditional PM machines, and also comparable to that of mechanical gearboxes.

Magnetic-geared permanent magnet machine (MGPM) is a novel derivation of MGs. By integrating a PM machine into a MG or vice versa, new mechanisms can be developed, which are able to achieve electromechanical energy conversion. MGs can reduce the rotational speeds of PM machines as well as increase their output torques, therefore, MGPMs are capable of offering low-speed large-torque operation. It means that they can get rid of mechanical gearboxes in many occasions, such as wind power generation, electric power propulsion, industrial robot drive and so forth. Due to the large torque density of MGs, MGPMs become rather promising competitors in the family of direct-drive machines[9-11]. According to the deployment of the armature stator, MGPMs can be generally classified into three types, viz., MGPM with inner armature stator(MGPM-IAS)[12-15], MGPM with outer armature stator(MGPM-OAS)[16-17], and MGPM with sandwiched armature stator (MGPM-SAS)[18]. It is worth noting that there are two stators engaged in the MGPM-IAS, one is the armature stator, and the other is the modulating stator. Herein, the armature stator refers to the component on which the armature windings are equipped. In addition, two PM machines which are also derived from MGs have been reported in [19-21]. However, we cannot observe a complete MG with two PM rotors in these machines.

From the 'power-flow-path' point of view, for the aforementioned three types of MGPMs, our investigation finds out that there are parallel-path power flows in the MGPM-SAS and MGPM-OAS when they achieve electromechanical energy conversion, but the

* Corresponding Author, E-mail: jianln@sustc.edu.cn.
Supported in part by the National Natural Science Foundation of China under Grant 51377158, by the Natural Science Foundation of Guangdong Province under Project 2014A030306034, 2015TQ01N332, and by the Science and Technology Innovation Committee of Shenzhen under Projects ZDSYS201604291912175, and JCYJ20150529152146473.

MGPM-SAS is better suited to capitalize on the potential parallel path power flows than the MGPM-OAS. And this phenomenon does not exist in MGPM-IAS. The parallel-power-flow-path results in the MGPM-SAS having greater potential to offer even higher output torque than its integrated MG. The purpose of this paper is to elaborate this issue in MGPM-SAS. Three typical MGPMs and their power flow paths will be introduced in section 2. Next, the parallel-power-flow-path is analyzed from the aspect of electromagnetic fields interaction in section 3. After that, simulation analysis and experimental verification are presented in section 4 and 5, respectively. Finally, the conclusions are drawn in section 6.

2 Three typical MGPMs and their power flow paths

2.1 MGPM-IAS

Fig.1 depicts the cross-sectional view of the MGPM-IAS. It consists of two rotors, two stators and three air-gaps. The outer rotor, the modulating stator and the inner rotor constitute a MG. The inner rotor and the inner armature stator constitute a PM machine. PM poles are placed on both the inner rotor and the outer rotor. The sum of the pole-pair numbers(PPNs) of these two rotors is equal to the number of ferromagnetic segments equipped on the modulating stator. Therefore, the MG can achieve stable magnetic torque transmission between the two rotors, and the ratio of their rotational speeds is equal to the ratio of their PPNs. The outer rotor is also known as low-speed rotor since it has more PM poles, while the inner rotor is also called high-speed rotor. The armature windings are deployed on the inner armature stator, and their PPN is designed to be equal to that of the inner rotor PM poles.

Fig.2 illustrates the power flow path in the MGPM-IAS. Since the PPN of the armature windings is the same with that of the inner rotor, the armature field generated by the stator currents can interact with the PM poles placed on the inner rotor, so as to achieve stable electromechanical energy conversion. When the MGPM-IAS works as a motor, the inner rotor is driven by the stator currents, and rotates at relatively high speed. Then, with the help of the modulating stator, the

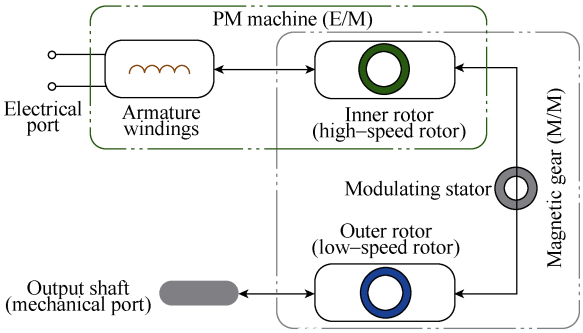

Fig.2 Power flow path in MGPM-IAS

mechanical power of the inner rotor is transmitted to the outer rotor. Due to the function of the integrated MG, large output torque and low rotational speed can be obtained at the mechanical port. When the MGPM-IAS works as a generator, mechanical power is input from the mechanical port, and then transmitted to the inner rotor. After that, the rotating magnetic field excited by the inner rotor PM poles can couple with the armature windings to generate electrical power. Apparently, these are serial-path power flows. This means that no matter whether it works as a motor or a generator, the maximum output/input torque of MGPM-IAS is limited by the torque transmission capability of its integrated MG.

2.2 MGPM-OAS

Fig.3 depicts the cross-sectional view of the MGPM-OAS. It consists of one stator, two rotors and two air-gaps. PM poles are located on both the stator and the inner rotor. The integrated MG is a little bit different from that in the MGPM-IAS, and the modulating ring becomes the low-speed outer rotor. The sum of the PPNs of PM poles engaged on the stator and the inner rotor is equal to the number of ferromagnetic segments equipped on the modulating ring(outer rotor). The armature windings are deployed on the outer armature stator, and its PPN is designed to be equal to that of the inner rotor PM poles.

Fig.4 illustrates the power flow path in MGPM-OAS. The armature windings can interact with the inner rotor to achieve stable electromechanical energy conversion, and they constitute PM machine I. Meanwhile, the magnetic field generated by armature currents also can interact with the field excited by stator PMs by flux modulation effect of modulating ring.

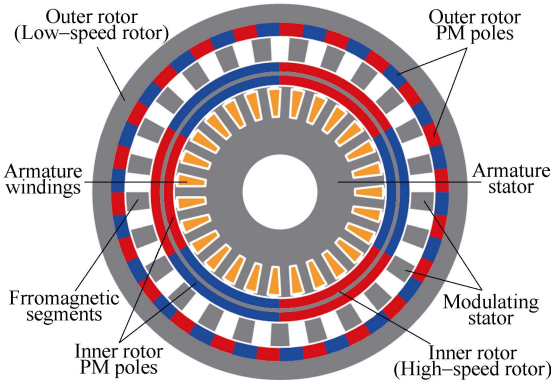

Fig.1 Cross-sectional view of MGPM-IAS

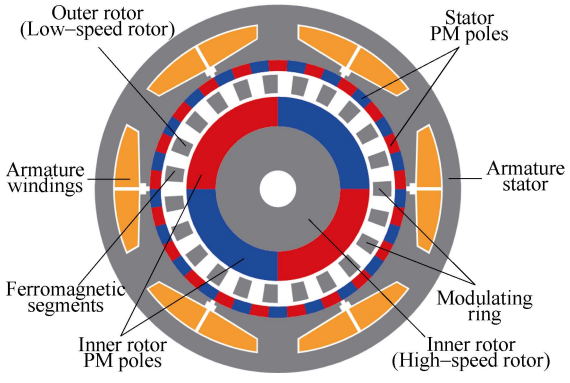

Fig.3 Cross-sectional view of MGPM-OAS

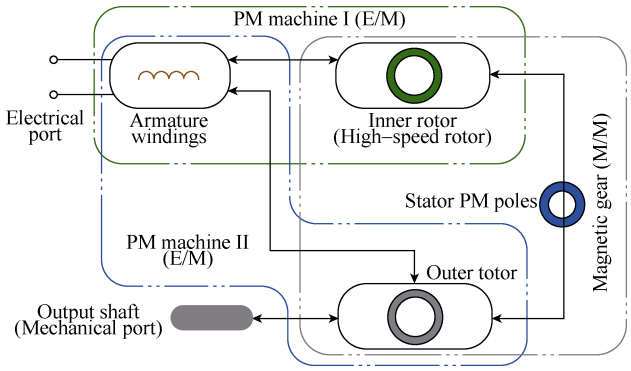

Fig.4 Power flow path in MGPM-OAS

Thus, the armature stator with windings, stator PM poles and modulating ring constitute PM machine II, which is called stator-excited vernier PM machine[22]. When it works as a motor, the inner rotor is driven by the stator currents, and rotates at relatively high speed. Then, with the help of its integrated MG, the mechanical power of the inner rotor is transmitted to the modulating ring(outer rotor), moreover, the outer rotor can be directly driven by the armature currents simultaneously due to flux modulation effect, and finally MGPM-OAS outputs to drive the mechanical loads through two power flow paths. When the MGPM-OAS works as a generator, mechanical power is input from the mechanical port, and return along the original paths in motor condition. Finally, electrical power can be generated with the armature windings. It can be observed that the power-flow-path existing in the MGPM-OAS is parallel. However, PMs are located in both inner and outer air-gaps, since the relative permeability of PMs and air is very close, it is equivalent to increasing the length of the two air-gaps. Especially for PM machine II, it is bound to affect the flux modulation effect and weaken the magnitude of the dominant harmonic. Therefore, it is more likely that most of the power flows through PM machine I and its MG.

2.3 MGPM-SAS

Fig.5 depicts the cross-sectional view of the MGPM-SAS. It consists of one stator, two rotors and two air-gaps. PM poles are mounted on both the outer rotor and the inner rotor. In this case, the interior PM design is adopted on the inner rotor. The armature windings are deployed among the air slots of the modulating ring which is sandwiched in-between the two rotors. Thus, the modulating ring of the integrated MG also serves as the armature stator of the whole machine. The sum of the PPNs of PM poles engaged on the two rotors is equal to the number of ferromagnetic segments equipped on the modulating ring (armature stator). The PPN of the armature windings is designed to be equal to that of the inner rotor PM poles.

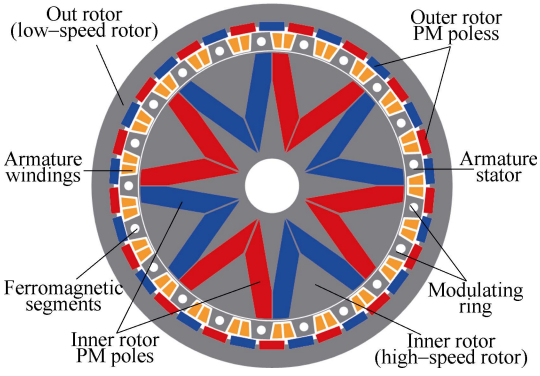

Fig.5 Cross-sectional view of MGPM-SAS

Fig.6 illustrates the power flow path in MGPM-SAS. It is quite natural to understand that the armature stator and the inner rotor can interact with each other to achieve stable electromechanical energy conversion. That is the first PM machine(PM machine I) integrated in the MGPM-SAS. It is worth noting that, although the PPN of armature windings is equal to that of the inner rotor PM poles, one of the field harmonics excited by the armature currents with the help of the modulating ring has the same PPN with that of the PM poles equipped on the outer rotor. This means the armature windings can also interact with the outer rotor to achieve stable electromechanical energy conversion. That is the second PM machine (PM machine II) integrated in the MGPM-SAS. In much literature, this kind of machine is termed as harmonic machine or vernier machine[23].When the MGPM-SAS works as a motor, on one path the inner rotor is driven by the stator currents, and then, with the help of the modulating stator, the mechanical power is transmitted to the outer rotor, while on the other path the outer rotor is directly driven by the stator currents. When the MGPM-SAS works as a generator, the input mechanical power can also flow two paths, and be converted to electrical power by the armature windings. Very typically, these are parallel-path power flows, and they allow the MGPM-SAS to have the possibility to output or input mechanical torques higher than the torque transmission capability of its integrated MG. Compared with MGPM-OAS, the slots of the modulating ring are fully used by the armature windings, which can save lots of space and reduce the volume. What's the most important is that the topology of the MGPM-SAS does not affect the length of the air-gaps. Hence, the MGPM-SAS is better suited to capitalize on the potential parallel path power flows than the MGPM-OAS.

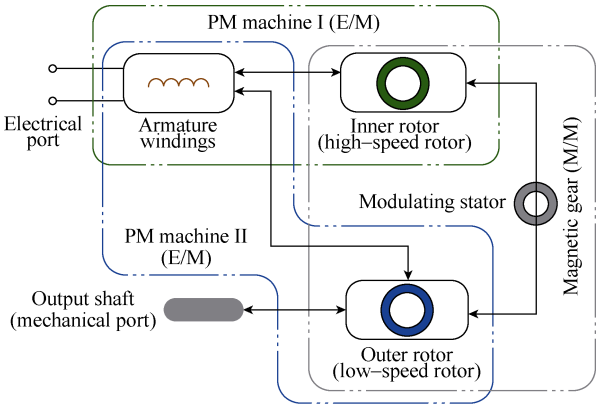

Fig.6 Power flow path in MGPM-SAS

2.4 Summary

- The MGPM-IAS is with the most complicated mechanical structure among the three typical MGPMs. It has four concentric components which are divided by three air-gaps. This presents a big challenge to its manufacturing and assembling. The power-flow-path in MGPM-IAS is serial, and its maximum output/input torque is limited by the torque transmission capability of the integrated MG.
- The MGPM-OAS is with the least complicated mechanical structure among the three typical MGPMs. Its outer armature stator and inner rotor topology bring convenience to its manufacturing and assembling. However, the mechanical strength of its rotational modulating ring (outer rotor) remains a troublesome issue. Although the power-flow-path in MGPM-OAS is parallel, it is more likely that the effect of parallel-path is poor, and most of power flows through one of the path.
- The mechanical structure of MGPM-SAS is a little more complicated than that of MGPM-OAS, yet still, more compact than that of MGPM-IAS. The armature windings are embedded in the modulating ring, and do not occupy extra space. Unlike the MGPM-IAS, MGPM-SAS has parallel-path power flows, which allow the MGPM-SAS having the possibility to offer even higher output torque than its integrated MG. Compared with the MGPM-OAS, MGPM-SAS can achieve parallel-path power flows better than MGPM-OAS. So the paper below will focus on the analyses of the MGPM-SAS.

3 Interaction of electromagnetic fields in MGPM-SAS

3.1 Magnetic torque transmission

Firstly, the magnetic torque transmission between the inner rotor and the outer rotor is investigated. It's well known that the MG is able to achieve torque transmission and speed variation as long as the following equation is satisfied,

$$N_s = P_{in} + P_{out} \tag{1}$$

where P_{in} and P_{out} are the PPNs of the PM poles placed on the inner rotor and the outer rotor, respectively, and N_s is the number of ferromagnetic segments on the modulating ring.

As illustrated in Fig.7, a polar coordinate is built on the modulating ring which is stationary in the MGPM-SAS. The assumed positive direction is counterclockwise. The magnetic field fundamental component $B^{in}_{(1,0)}$ generated by the inner rotor PM poles can be expressed as,

$$B^{in}_{(1,0)} = k_{in}\cos\left(P_{in}\left(\theta - \theta^{in}_{(1,0)}\right)\right) \tag{2}$$

where k_{in} denotes the magnitude of the field fundamental component, and $\theta^{in}_{(1,0)}$ indicates its position. Moreover, $\theta^{in}_{(1,0)}$ also represents the position of the inner rotor.

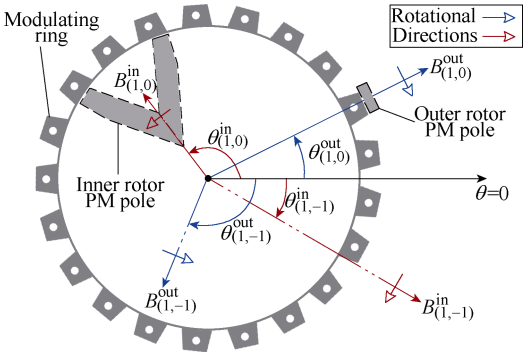

Fig.7 Interaction of magnetic fields in integrated MG

The major harmonic field component $B^{in}_{(1,-1)}$ excited by the modulating ring can be obtained as [24],

$$B^{in}_{(1,-1)} = k'_{in}\cos\left(P_{out}\left(\theta + \theta^{in}_{(1,-1)}\right)\right) \tag{3}$$

where k'_{in} and $\theta^{in}_{(1,-1)}$ refer to the magnitude and the position of this field harmonic component, respectively. It can be observed that $B^{in}_{(1,-1)}$ has exactly the same PPN with the outer rotor PM poles, and its position can be determined by,

$$\theta^{in}_{(1,-1)} = \frac{P_{in}}{P_{out}}\theta^{in}_{(1,0)} \tag{4}$$

Similarly, the magnetic field fundamental component $B^{out}_{(1,0)}$ generated by the outer rotor PM poles can be expressed as,

$$B^{out}_{(1,0)} = k_{out}\cos\left(P_{out}\left(\theta - \theta^{out}_{(1,0)}\right)\right) \tag{5}$$

where k_{out} and $\theta^{out}_{(1,0)}$ denote its magnitude and position, respectively. In addition, $\theta^{out}_{(1,0)}$ also represents the position of the outer rotor.

The major harmonic field component $B^{out}_{(1,-1)}$ excited by the modulating ring can be given by,

$$B^{out}_{(1,-1)} = k'_{out}\cos\left(P_{in}\left(\theta + \theta^{out}_{(1,-1)}\right)\right) \tag{6}$$

where k'_{out} and $\theta^{out}_{(1,-1)}$ refer to its magnitude and position, respectively. It can also be observed that $B^{out}_{(1,-1)}$ has exactly the same PPN with the inner rotor PM poles, and its position can be determined by,

$$\theta^{out}_{(1,-1)} = \frac{P_{out}}{P_{in}}\theta^{out}_{(1,0)} \tag{7}$$

From (2), (6) and (7), it can be known that the magnetic torque T^{in}_{PM} which is exerted on the inner rotor and produced by the interaction of $B^{in}_{(1,0)}$ and $B^{out}_{(1,-1)}$ can be expressed by,

$$T^{in}_{PM} = -w_1 \sin P_{in}\left(\theta^{in}_{(1,0)} + \theta^{out}_{(1,-1)}\right) = -w_1 \sin\left(P_{in}\theta^{in}_{(1,0)} + P_{out}\theta^{out}_{(1,0)}\right) \tag{8}$$

And from (3), (4) and (5), the magnetic torque T^{out}_{PM} exerted on the outer rotor due to the coupling of

$B^{\text{out}}_{(1,0)}$ and $B^{\text{in}}_{(1,-1)}$ can be given by,

$$T^{\text{out}}_{\text{PM}} = -w_2 \sin P_{\text{out}}\left(\theta^{\text{out}}_{(1,0)} + \theta^{\text{in}}_{(1,-1)}\right) = -w_2 \sin\left(P_{\text{in}}\theta^{\text{in}}_{(1,0)} + P_{\text{out}}\theta^{\text{out}}_{(1,0)}\right) \tag{9}$$

where w_1 and w_2 refer to the magnitudes of $T^{\text{in}}_{\text{PM}}$ and $T^{\text{out}}_{\text{PM}}$, respectively.

Both (8) and (9) indicate that the magnetic torques $T^{\text{in}}_{\text{PM}}$ and $T^{\text{out}}_{\text{PM}}$ transmitted by the integrated MG are determined by the relative position between the two rotors. In order to achieve stable torque transmission, the term $P_{\text{in}}\theta^{\text{in}}_{(1,0)} + P_{\text{out}}\theta^{\text{out}}_{(1,0)}$ should be kept as constant, which means,

$$G_{\text{r}} = \frac{\Omega_{\text{in}}}{\Omega_{\text{out}}} = -\frac{P_{\text{out}}}{P_{\text{in}}} \tag{10}$$

where G_{r} is the gear ratio, Ω_{in} and Ω_{out} are the rotational speeds of the inner rotor and the outer rotor, respectively, and the minus sign implies that the two rotors should rotate in opposite directions.

3.2 Electromechanical energy conversion

Secondly, the electromechanical energy conversion among the armature windings and the two rotors are discussed. As illustrated in Fig.8, the electromagnetic field fundamental component $B^{\text{aw}}_{(1,0)}$ generated by the armature windings can be expressed as,

$$B^{\text{aw}}_{(1,0)} = k_{\text{aw}} \cos\left(P_{\text{aw}}\left(\theta - \theta^{\text{aw}}_{(1,0)}\right)\right) \tag{11}$$

where k_{aw} and $\theta^{\text{aw}}_{(1,0)}$ denote its magnitude and position, respectively. P_{aw} is the PPN of the armature windings, and it is equal to that of the inner rotor PM poles P_{in}.

When injecting AC currents into the armature windings, the rotational speed of $B^{\text{aw}}_{(1,0)}$ is determined by,

$$\Omega^{\text{aw}}_{(1,0)} = \frac{2\pi f}{P_{\text{aw}}} = \frac{2\pi f}{P_{\text{in}}} \tag{12}$$

where f is the frequency of the injected ac currents, and $\Omega^{\text{aw}}_{(1,0)}$ is the synchronous speed of the integrated PM machine I. When the inner rotor is rotating at this speed, namely,

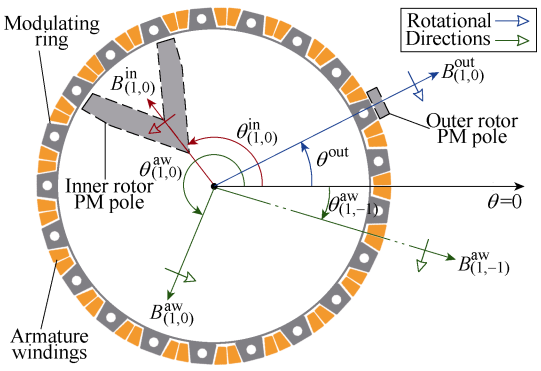

Fig.8 Interaction of electromagnetic fields in integrated PM machines

$$\Omega_{\text{in}} = \Omega^{\text{aw}}_{(1,0)} \tag{13}$$

stable electromechanical energy conversion can be achieve by the coupling of field components $B^{\text{in}}_{(1,0)}$ and $B^{\text{aw}}_{(1,0)}$. The resulted electromagnetic torque exerted on the inner rotor can be expressed as,

$$T^{\text{in}}_{\text{EM}} = w_3 \sin P_{\text{in}}\left(\theta^{\text{aw}}_{(1,0)} - \theta^{\text{in}}_{(1,0)}\right) \tag{14}$$

where w_3 denotes the magnitudes of $T^{\text{in}}_{\text{EM}}$.

In addition, the major harmonic field component $B^{\text{aw}}_{(1,-1)}$ excited by the armature windings and the modulating ring can be given as,

$$B^{\text{aw}}_{(1,-1)} = k'_{\text{aw}} \cos\left(P_{\text{out}}\left(\theta + \theta^{\text{aw}}_{(1,-1)}\right)\right) \tag{15}$$

$$\theta^{\text{aw}}_{(1,-1)} = \frac{P_{\text{in}}}{P_{\text{out}}}\theta^{\text{aw}}_{(1,0)} \tag{16}$$

where k'_{aw} and $\theta^{\text{aw}}_{(1,-1)}$ refer to the magnitude and the position of this field harmonic component, respectively. It can be observed that $B^{\text{aw}}_{(1,-1)}$ has exactly the same PPN with $B^{\text{out}}_{(1,0)}$. Moreover, they revolve synchronously. Therefore, the coupling of these two field components is able to achieve stable electromechanical energy conversion as well. That is how the integrated PM machine II works, and the resulting electromagnetic torque exerted on the outer rotor can be expressed as,

$$T^{\text{out}}_{\text{EM}} = -w_4 \sin P_{\text{out}}\left(\theta^{\text{aw}}_{(1,-1)} + \theta^{\text{out}}_{(1,0)}\right) = -w_4 \sin\left(P_{\text{in}}\theta^{\text{aw}}_{(1,0)} + P_{\text{out}}\theta^{\text{out}}_{(1,0)}\right) \tag{17}$$

where w_4 denotes the magnitudes of $T^{\text{out}}_{\text{EM}}$.

3.3 Torque capability of MGPM-SAS

Thirdly, the output torque capability of the MGPM-SAS is investigated. After the MGPM-SAS enters stable state, the rotational speeds of the two rotors remain unchanged, and the total torque working on the inner rotor $T^{\text{in}}_{\text{total}}$ should be equal to zero, namely,

$$T^{\text{in}}_{\text{total}} = T^{\text{in}}_{\text{EM}} + T^{\text{in}}_{\text{PM}} = 0 \tag{18}$$

By substituting (8) and (14) into (18) gets,

$$w_3 \sin P_{\text{in}}\left(\theta^{\text{aw}}_{(1,0)} - \theta^{\text{in}}_{(1,0)}\right) = w_1 \sin\left(P_{\text{in}}\theta^{\text{in}}_{(1,0)} + P_{\text{out}}\theta^{\text{out}}_{(1,0)}\right) \tag{19}$$

Then, the total torque working on the outer rotor $T^{\text{out}}_{\text{total}}$ can be given by,

$$T^{\text{out}}_{\text{total}} = T^{\text{out}}_{\text{EM}} + T^{\text{out}}_{\text{PM}} \tag{20}$$

By substituting (9) and (17) into (20) gets,

$$T^{\text{out}}_{\text{total}} = -\left[w_4 \sin\left(P_{\text{in}}\theta^{\text{aw}}_{(1,0)} + P_{\text{out}}\theta^{\text{out}}_{(1,0)}\right) + w_2 \sin\left(P_{\text{in}}\theta^{\text{in}}_{(1,0)} + P_{\text{out}}\theta^{\text{out}}_{(1,0)}\right)\right] \tag{21}$$

where the minus sign indicates that its direction is opposite to the assumed positive direction, and it will

drive the outer rotor to rotate clockwise.

The peak output torque capability can be examined by locking the outer rotor, for example, letting $\theta_{(1,0)}^{\text{out}}=0$. Then, (19) and (21) become,

$$w_3 \sin P_{\text{in}}\left(\theta_{(1,0)}^{\text{aw}}-\theta_{(1,0)}^{\text{in}}\right)=w_1 \sin\left(P_{\text{in}}\theta_{(1,0)}^{\text{in}}\right) \tag{22}$$

$$T_{\text{total}}^{\text{out}}=-\left(w_4 \sin\left(P_{\text{in}}\theta_{(1,0)}^{\text{aw}}\right)+w_2 \sin\left(P_{\text{in}}\theta_{(1,0)}^{\text{in}}\right)\right) \tag{23}$$

with the position angle $\theta_{(1,0)}^{\text{aw}}$ increasing incrementally, the balance position of the inner rotor $\theta_{(1,0)}^{\text{in}}$ can be determined by (22), and the output torque $T_{\text{total}}^{\text{out}}$ can be gotten from (23). The peak point of the $T_{\text{total}}^{\text{out}}-\theta_{(1,0)}^{\text{aw}}$ curve represents the maximum output torque of MGPM-SAS. Obviously, the maximum output torque is affected by the coefficients w_3 and w_4, which are both related to the magnitude of the injected ac currents. It can also be derived from (23) that the maximum value of $T_{\text{total}}^{\text{out}}$ is possible to exceed the maximum pull-out torque of its integrated MG which is denoted by the coefficient w_2 in (23).

4 Simulation analysis

Simulation analysis of the investigated MGPM-SAS is conducted by using two-dimensional finite element method (2D-FEM). Its specifications are listed in Table 1. The slots and winding connections are given in Fig.9. The PPN of the inner rotor PM poles and the outer rotor PM poles are 4 and 17, respectively. Thus, according to (10) the gear ratio of its integrated MG should be -4.25:1.

Table 1 Specifications of investigated MGPM-SAS

Number of ferromagnetic segments / armature slots	21
PPNs of inner rotor PM poles / armature windings	4
PPNs of outer rotor PM poles	17
Relative permeability of PMs	1.05
Remanence of PM poles/T	1.3
Material of stator and rotors	50H600
Number of Phases	3
Radius of outer rotor/mm	100
Length of inner air-gap / outer air-gap/mm	0.6
Stack length/mm	60
Thickness of outer rotor PM poles/mm	5
Thickness of inner rotor PM poles/mm	10

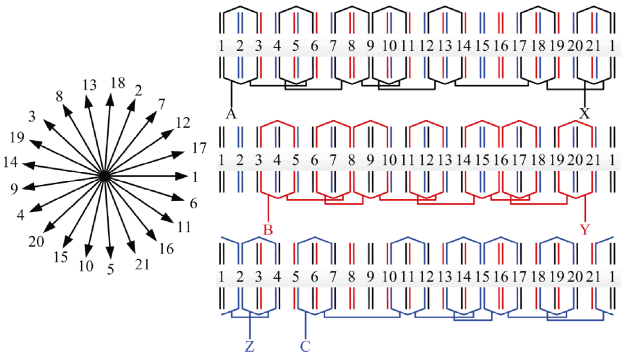

Fig.9 Slots and winding connections

In order to find out the field coupling among armature windings, inner rotor and outer rotor, field analyses of MGPM-SAS are performed by 2D-FEM. The magnetic fields excited by inner rotor (Case I), outer rotor (Case II) and armature windings (Case III) are analyzed in turn. Herein, the magnitude of the currents I_a is equal to 10.0 A. Fig.10 shows the flux lines of the three cases. It can be observed from Fig.10(a) that due to the effect of flux-focus caused by the 'V-shaped' PMs in inner rotor, plenty of flux lines can reach the outer rotor across the modulating ring. As shown in Fig.10(b) and Fig.10(c), regardless of case II and case III, there are few flux lines going through inner rotor. Fig.11, Fig.12, and Fig. 13 exhibit the radial flux density waves in the middle of the two air-gaps and their harmonic spectra in the three cases. It can be seen from Fig.11 to Fig.13 that the dominant harmonics in case I and III are those with PPN=4, while the harmonics with PPN=17 play dominant

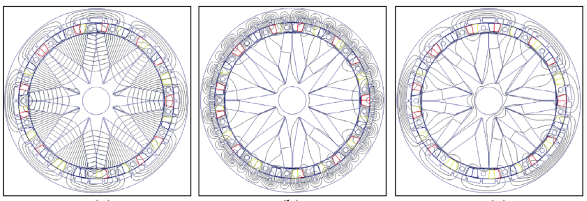

Fig.10 Flux lines: (a) case I: field excited by PMs on inner rotor (b) case II: field excited by PMs on outer rotor (c) case III: field excited by armature current

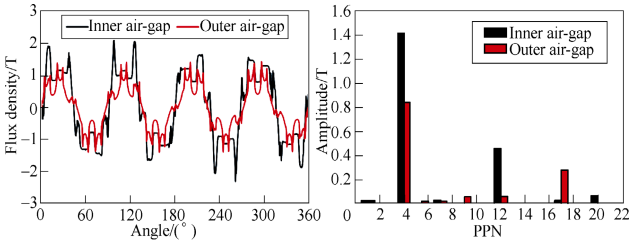

(a) Flux density waves in inner and outer air-gaps (b) Harmonic spectra

Fig.11 Field analyses of case I

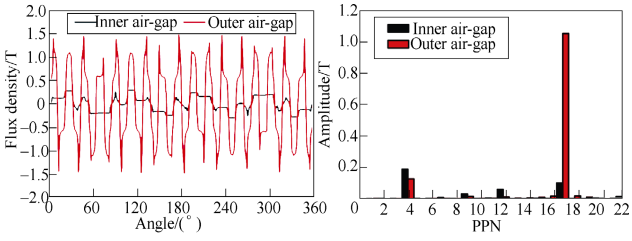

(a) Flux density waves in inner and outer air-gaps (b) Harmonic spectra

Fig.12 Field analyses of case II

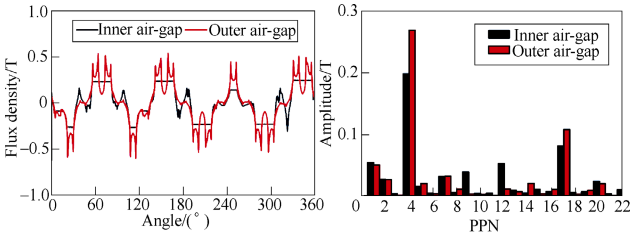

(a) Flux density waves in inner and outer air-gaps (b) Harmonic spectra

Fig.13 Field analyses of case III

roles in case II. For case I and III, these dominant harmonics can interact with each other to achieve stable energy conversion and this is how PM machine I in MGPM-SAS works. Moreover, judging by Fig.13(b), for armature windings, the amplitude of the harmonics with PPN=17 in outer air-gap is the second largest one. The harmonics can also couple with the dominant ones generated by outer rotor to make a contribution to stable energy conversion and this is how PM machine II in MGPM-SAS works.

In order to figure out the performance of the two integrated PM machines, the induced back EMF waveforms are calculated. Firstly, the outer rotor PM poles are removed, and the rotational speed of inner rotor Ω_{in} is set as 425r/min. Consequently, the calculated back EMFs of the armature windings are illustrated in Fig.14. The horizontal axis represents the inner rotor position, which is indicated as $\theta^{in}_{(1,0)}$ in Fig.8. It can be observed that the magnitude and the frequency of the induced back EMFs are 191.4V and 28.33Hz, respectively.

Secondly, the inner rotor PM poles are removed, and the rotational speed of outer rotor Ω_{out} is set as −100r/min. Herein, the minus sign implies the outer rotor revolves in clockwise direction. The calculated back EMFs of the armature windings are illustrated in Fig.15. The horizontal axis represents the outer rotor position, which is indicated as $\theta^{out}_{(1,0)}$ in Fig.8. It can be known that the magnitude and the frequency of the induced back EMFs are 64.8V and 28.33Hz, respectively.

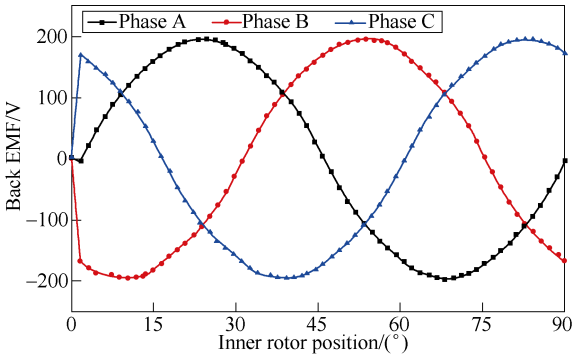

Fig.14 Back EMF waveforms induced by integrated PM machine I

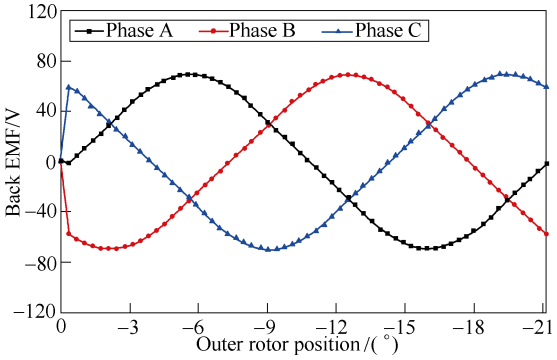

Fig.15 Back EMF waveforms induced by integrated PM machine II

Thirdly, both the inner rotor PM poles and the outer rotor PM poles are taken into account. The rotational speeds of the two rotors are set as Ω_{in}=425 r/min and Ω_{out}=−100 r/min, respectively. The obtained waveforms are presented in Fig.16, in which the positions of the two rotors are indicated simultaneously. It can be known that the magnitude and the frequency of back EMFs induced by the two PM rotors are 223.7V and 28.33Hz, respectively.

The results of Fig.14, Fig.15, and Fig.16 are quantitatively compared in Table 2. The frequencies of waveforms in all three cases are the same and equal to 28.33 Hz, which matches (12) very well. It also demonstrates that the integrated PM machines I and II can achieve electromechanical energy conversion at exactly the same pace. This is vitally important to the effectiveness of the aforementioned parallel power-flows in the MGPM-SAS. The total harmonic distortion (THD) are also listed, which shows that the back EMF waveforms induced by PM machine I is more sinusoidal than those induced by PM machine II. The magnitude of back EMFs induced by PM machine I is much higher than that induced by PM machine II. This implies the integrated PM machine I makes dominant contribution to the electromechanical energy conversion of the MGPM-SAS. By adding the results presented in Fig.14 and Fig.15, the obtained magnitude of back EMFs is equal to 256.2V. It is about 10% higher than the magnitude of waveforms presented in Fig.16. This is caused by the nonlinear characteristics of the iron cores. If we assume the iron materials having linear *B-H* characteristic in the FEM model, the calculation results are also listed in Table 2. It can be found that the results of 'PM machine I+II' are very close to those of 'MGPM-SAS'.

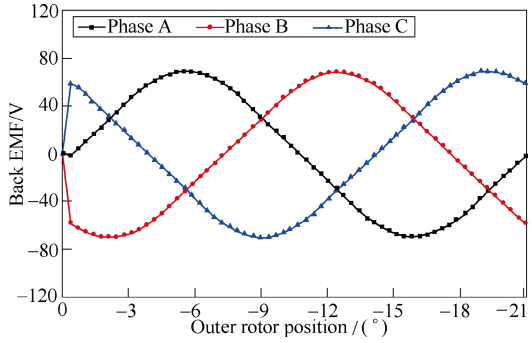

Fig.16 Back EMF waveforms induced by MGPM-SAS

Table 2 Results of calculated back EMFs

Model with nonlinear iron material			
	Magnitude/V	Frequency/Hz	THD(%)
PM machine I	191.4	28.33	3.69
PM machine II	64.8	28.33	5.07
PM machine I+II	256.2	28.33	3.26
MGPM-SAS	223.7	28.33	3.05
Model with linear iron material (Assumed)			
	Magnitude/V	Frequency/Hz	THD(%)
PM machine I	214.8	28.33	3.42
PM machine II	74.3	28.33	4.89
PM machine I+II	289.1	28.33	3.01
MGPM-SAS	288.7	28.33	2.93

The torque transmission capability of the integrated MG is assessed. By locking the outer rotor at the position $\theta_{(1,0)}^{\text{out}}=0$, and rotating the inner rotor incrementally, we can get the magnetic torque curves as shown in Fig.17. The horizontal axis represents the inner rotor position $\theta_{(1,0)}^{\text{in}}$. It can be observed that the shape of the two curves match (8) and (9) very well. Moreover, the peak torque values on the inner rotor and the outer rotor are 75.5N·m and 320.8N·m, respectively, which means the coefficient w_1 in (8)equals 75.5, and the coefficient w_2 in (9) equals 320.8.

The electromagnetic torque capabilities of the two integrated PM machines are also assessed. Firstly, the two rotors are locked at the positions $\theta_{(1,0)}^{\text{out}}=0$ and $\theta_{(1,0)}^{\text{in}}=0$. Then, three-phase symmetrical AC currents are injected into the armature windings. The magnitude of the currents I_a is equal to 10.0A. Finally, the resulted torque-angle curves are obtained as shown in Fig.18. The horizontal axis represents the position of the armature field vector which is denoted by $\theta_{(1,0)}^{\text{aw}}$ in Fig.8. It can be observed that the shape of the two curves match (14) and (17) very well. The peak torque values on the inner rotor and the outer rotor are 87.2N·m and 69.9N·m, respectively. This means that the coefficient w_3 in (14) equals 87.2, and the coefficient w_4 in (17) equals 69.9. It should be noted that the two coefficients are strongly related to the magnitude of the injected AC currents. Without considering the saturation of the iron cores, if the injected currents are increased, the resultingvalues of the two coefficients will be higher.

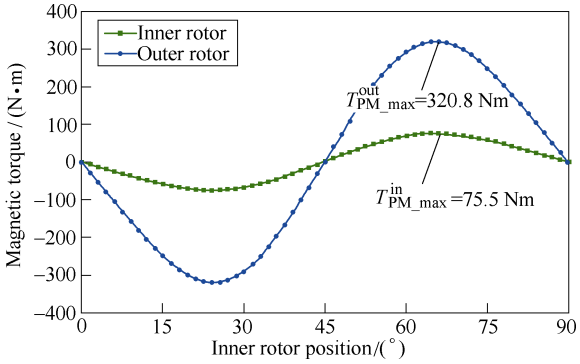

Fig.17 Magnetic torque curves when locking outer rotor

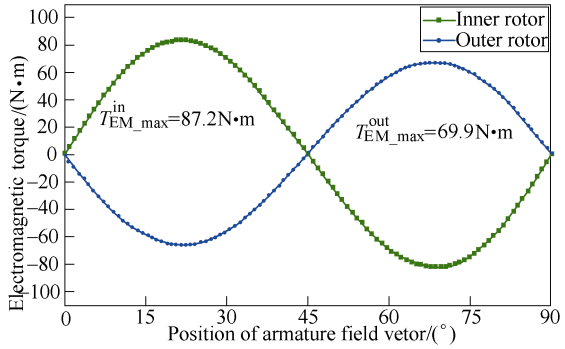

Fig.18 Electromagnetic torque curves when locking two rotors

As far as the torque capability of MGPM-SAS is concerned, the output torques on the outer rotor is calculated when locating the armature field vector $B_{(1,0)}^{\text{aw}}$ at different positions. As shown in Fig.19, the outer rotor is kept standstill at the position $\theta_{(1,0)}^{\text{out}}=0$, and the armature field position $\theta_{(1,0)}^{\text{aw}}$ is increased from 0° to 45° step by step. The balance positions of inner rotor $\theta_{(1,0)}^{\text{in}}$ are determined by (22). The results are also verified by using FEM, so as to make sure that the total torque working on the inner rotor $T_{\text{total}}^{\text{in}}$ is equal to zero. Finally, the output torque on the outer rotor $T_{\text{total}}^{\text{out}}$ can be obtained by using FEM. As indicated in (20) and (21), $T_{\text{total}}^{\text{out}}$ is composed of two parts, in which $T_{\text{EM}}^{\text{out}}$ represents the electromagnetic torque produced by the integrated PM machine II, and $T_{\text{PM}}^{\text{out}}$ refers to the magnetic torque transmitted by the integrated MG. It can be observed that $T_{\text{PM}}^{\text{out}}$ makes dominant contribution to $T_{\text{total}}^{\text{out}}$, while $T_{\text{EM}}^{\text{out}}$ just plays a subsidiary role. Nevertheless, due to the existence of $T_{\text{EM}}^{\text{out}}$, the MGPM-SAS is able to offer even higher output torque than its integrated MG. As illustrated in Fig.19, the maximum output torque on outer rotor reaches 351.2N·m, which is about 10% larger than the maximum output torque of the integrated MG shown in Fig.17. In this case, the position angle of armature field $\theta_{(1,0)}^{\text{aw}}$ and the corresponding balance position of inner rotor $\theta_{(1,0)}^{\text{in}}$ are 34° and 20°, respectively. Therefore, the spatial position relationship of these involved magnetic field vectors can be illustrated by Fig.20.

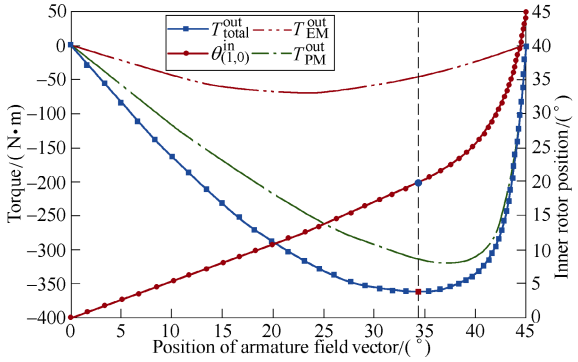

Fig.19 Output torques of outer rotor and balance positions of inner rotor with different positions of armature field vector when locking outer rotor

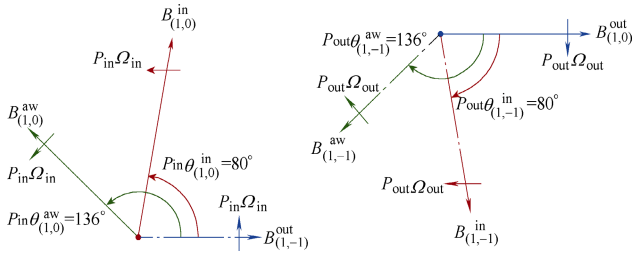

(a) Field vectors working on inner rotor (b) Field vectors working on outer rotor

Fig.20 Spatial position relationship among magnetic field vectors when MGPM-SAS offering maximum output torque

Fig.21 shows the calculated maximum output torques when injecting different armature currents. It can be observed that once the armature current is higher than 8 A, the MGPM-SAS is able to go beyond its integrated MG in terms of output torque capability. It is worth noting that when I_a is equal to 8A, the maximum electromagnetic torque of PM machine I is just equal to the maximum magnetic torque $T_{\mathrm{PM}}^{\mathrm{in}}$ which is exerted on the inner rotor, and this is a critical point. It can be seen from the color rectangle that $T_{\mathrm{EM}}^{\mathrm{out}}$ approaches zero and $T_{\mathrm{PM}}^{\mathrm{out}}$ is very close to $T_{\mathrm{total}}^{\mathrm{out}}$, which indicates that all the power almost flows through PM machine I and its integrated MG, then is transmitted to the outer rotor. Apart from the critical point, the two PM machine in MGPM-SAS work together to evidently fulfill parallel-path power flows. Especially when $I_a > 8$ A, it becomes more and more remarkable that PM machine II makes a contribution to the output torque.

5 Experimental verification

The investigated MGPM-SAS illustrated in Fig.5 and analyzed in section 4 is prototyped for experimental verification. The photos of its key components, steel laminations and the assembled test bed are shown in Fig.22.

Firstly, keep the out rotor freely rotatable, and drive the inner rotor by an induction motor. The output speed of the driving motor is set as 425r/min. Consequently, the resulting rotational speed of the outer rotor shaft is equal to −100r/min, which can match (10) very well. Fig.23 shows the measured back EMF waveforms of the armature windings. It can be observed that after the system enters stable stage, the measured frequency and magnitude of the back EMF are equal to 28.33Hz and 218.5V, respectively. Compared with the simulation results illustrated in Fig.16, it can be known that the measured frequency is exactly the same with that obtained by FEM calculation, moreover, the measured magnitude is very close to the calculated one, and the latter is equal to 223.7V.

Secondly, block the outer rotor and rotate the inner rotor step by step, the measured magnetic torques working on the inner rotor are shown in Fig.24(a). After that, block the inner rotor and incrementally rotate the outer rotor, the measured magnetic torques working on the outer rotor are shown in Fig.24(b). The calculated results are also presented in Fig.24 for comparison. The measured peak torques on inner rotor and outer rotor are 67.9N·m and 287.8N·m, respectively. They are about 10 % less than the calculated results. It

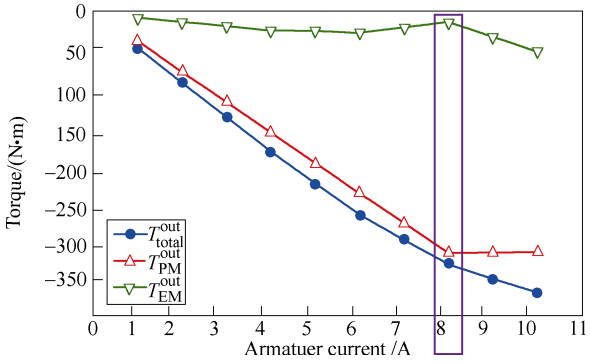

Fig.21 Maximum output torques on outer rotor when injecting different armature currents

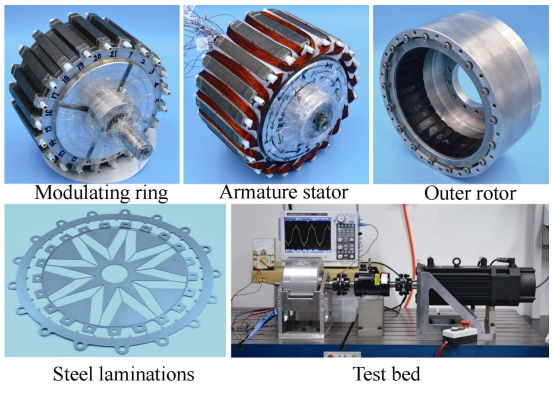

Fig.22 Prototype of investigated MGPM-SAS

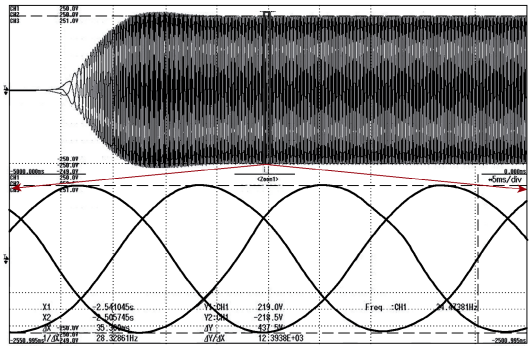

Fig.23 Measured back EMF waveforms

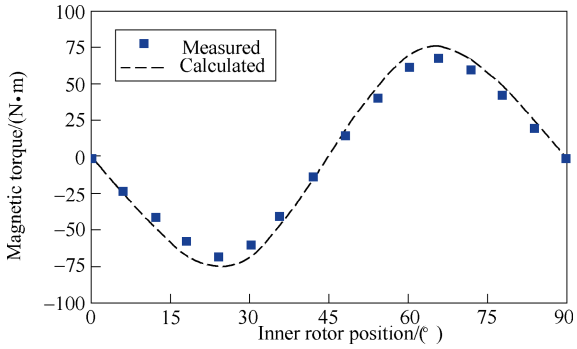

(a) Inner rotor

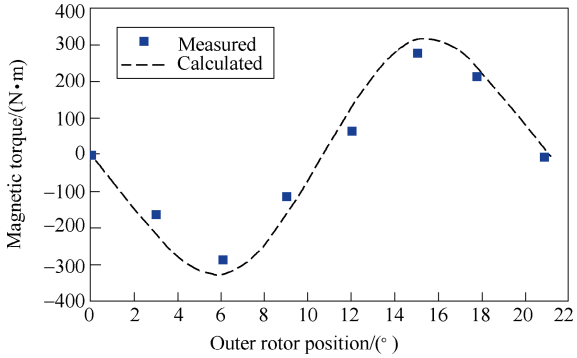

(b) Outer rotor

Fig.24 Comparison of measured and calculated torque capability of integrated MG

is well known that the 2D-FEM is incapable of taking into account the field leakage occurring in the edges. Therefore, the calculation results are usually higher than the real values.

Thirdly, connect the output shaft of MGPM-SAS to the induction motor, and feed the armature windings with AC currents. The induction motor is working as electric load of the MGPM-SAS. The measured maximum output torque on the outer rotor of MGPM-SAS at different armature currents are given in Fig.25. It can be observed that the measured results are close to the calculated values. Moreover, the MGPM-SAS can output 321.4N·m with I_a=10A, which is higher than the measured peak torque produced by the integrated MG. It demonstrates that the parallel-power-flow–path allows the MGPM-SAS having the possibility to offer even higher output torque than its involved MG.

It is necessary to point out that the screws sleeved by the white insulating tubes are used in the prototype in Fig.22, so as to ensure the mechanical strength of the modulating ring. Compared with simulation models without screws, the magnetic permittivity of the screws in the prototype is larger than that of air in simulation models, and this may be why there are little differences between the measured and calculated results.

6 Conclusion

In this paper, the power flow paths existing in MGPM-IAS, MGPM-OAS, and MGPM-SAS are discussed. The MGPM-IAS has just one power flow path and the torque capability is limited by the torque transmission capability of integrated MG. Although there exist parallel power flow paths in MGPM-OAS, compared with MGPM-SAS, MGPM-SAS is better suited to capitalize on the potential parallel path power flows. As well, the interaction of electromagnetic fields in MGPM-SAS is analyzed. The magnetic torque transmission offered by the integrated MG, and the electromechanical energy conversion achieved by the integrated PM machine I and II are elaborated. Both simulation calculations and experimental verifications are conducted. The results demonstrate that the MGPM-SAS has parallel-path power flows indeed and is able to offer higher output torque than its integrated MG.

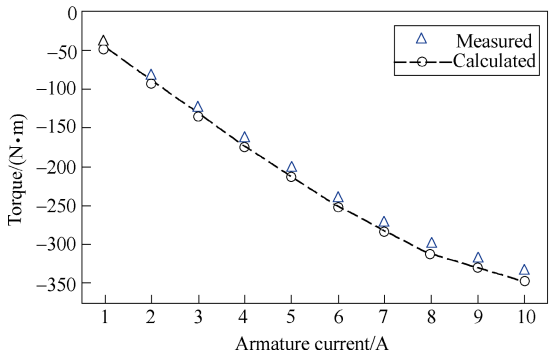

Fig.25 Comparison of measured and calculated maximum output torques on outer rotor when injecting different armature currents

References

[1] K. Atallah, and D. Howe, "A novel high-performance magnetic gear," *IEEE Trans. Magn.*, vol. 37, no. 4, pp. 2844-2846, Jul. 2001.

[2] N. Niguchi, and K. Hirata, "Cogging torque analysis of magnetic gear," *IEEE Trans. Ind. Electron.*, vol. 59, no. 5, pp. 2189-2197, May, 2012.

[3] S. Kim, C. Kim, S. Jung, and Y. Kim, "Optimal design of novel pole piece for power density improvement of magnetic gear using polynomial regression analysis," *IEEE Trans. Energy Convers*., vol. 30, no. 3, pp. 1171-1179, Sep., 2015.

[4] L. Jian, and K. T. Chau, "A coaxial magnetic gear with halbach permanent-magnet arrays," *IEEE Trans. Energy Convers.*, vol. 25, no. 2, pp. 319-328, Jun. 2010.

[5] K. Uppalapati, W. Bomela, J. Brid, M. Calvin, and J. Wright, "Experimental evaluation of low-speed flux-focusing magnetic gearboxes," *IEEE Trans. Ind. Appli.*, vol. 50, no.6, pp. 3637- 3643, 2014.

[6] R. Holehouse, K. Atallah, and J. Wang, "Design and realization of a linear magnetic gear," *IEEE Trans. Magn.*, vol. 47, no. 10, pp. 4171-4174, Oct. 2011.

[7] S. Afsari, H. Heydari, and B. Dianati, "Cogging torque mitigation in axial flux magnetic gear system based on skew effects using an improved quasi 3-d analytical method," *IEEE Trans. Magn.*, vol. 51, no. 9, Sep. 2015.

[8] L. Jian, G. Xu, J. Song, H. Xue, D. Zhao, and J. Liang, "Optimum design for improving modulating-effect of coaxial magnetic gear using response surface methodology and genetic algorithm," *Progr. Electromagn. Res.*, vol. 116, pp. 297-312, 2011.

[9] S. Debnath, J. Qin, and M. Saeedifard, "Control and stability analysis of modular multilevel converter under low-frequency operation," *IEEE Trans. Ind. Electron.*, vol. 62, no. 9, pp. 5329-5339, Sep., 2015.

[10] J. Holtz, G. Cunha, N. Petry, and P. Torri, "Control of large salient-pole synchronous machines using synchronous optimal pulse width modulation," *IEEE Trans. Ind. Electron.*, vol. 62, no. 6, pp. 3372-3379, Jun., 2015.

[11] W. Chu, Z. Q. Zhu, and J. Chen, "Simplified analytical optimization and comparison of torque densities between electrically excited and permanent-magnet machines," *IEEE Trans. Ind. Electron.*, vol.61, no.9, pp. 5000-5011, Sep., 2014.

[12] K. Chau, C. C. Chan, and C. Liu, "Overview of permanent-magnet brushless drives for electric and hybrid electric vehicles," *IEEE Trans. Ind. Electron.*, vol.55, no.6, pp. 2246-2257, Jun., 2008.

[13] L. Jian, K. Chau, and J. Jiang, "A magnetic-geared outer-rotor permanent-magnet brushless machine for wind power generation," *IEEE Trans. Ind. Appli.*, vol. 45, no.3, pp. 954-962, 2009.

[14] T. Frandsen, L. Mathe, N. Berg, R. Holm, T. Matzen, P. Rasmussen, and K. Jensen, "Motor integrated permanent magnet gear in a battery electrical vehicle," *IEEE Trans. Ind. Appli.*, vol. 51, no.2, pp. 1516–1525, 2015.

[15] S. Gerber, and R. Wang, "Design and evaluation of a magnetically geared PM machine," *IEEE Trans. Magn.*, vol. 51, no. 8, Aug. 2015.

[16] M. Bouheraoua, J. Wang, and K. Atallah, "Slip recovery and prevention in pseudo direct drive permanent-magnet machines," *IEEE Trans. Ind. Appli.*, vol. 51, no.3, pp. 2291-2299, 2015.

[17] J. Crider, and S. Sudhoff, "An inner rotor flux-modulated permanent magnet synchronous machine for low-speed high-torque applications," *IEEE Trans. Energy Convers.*, vol. 30, no. 3, pp. 1247-1254, Sep. 2015.

[18] L. Jian, W. Gong, G. Xu, J. Liang, and W. Zhao, "Integrated magnetic-geared machine with sandwiched armature stator for low-speed large-torque applications," *IEEE Trans. Magn.*, vol. 48, no. 11, Nov. 2012.

[19] Y. Fan, L. Zhang, J. Huang, and X. Han, "Design, analysis, and sensorless control of a self-decelerating permanent-magnet in-wheel motor," *IEEE Trans. Ind. Electron.*, vol. 61, no.10, pp. 5788-5797, Oct., 2014.

[20] J. Bai, P. Zheng, and C. Tong, "Characteristic analysis and verification of the magnetic-field-modulated brushless double-rotor machine," *IEEE Trans. Ind. Electron.*, vol. 62, no.7, pp. 4023-4032, Jul., 2015.

[21] L. Sun, M. Cheng, and H. Jian, "Analysis of a novel

magnetic-geared dual-rotor motor with complementary structure," *IEEE Trans. Ind. Electron.*, vol.62, no.11, pp. 6737-6747, Nov., 2015.
[22] L. Xu, G. Liu, W. Zhao, and J. Ji, "Stator-excited vernier high-temperature superconducting machine for direct drive propulsion," *IEEE Trans. Appl. Supercond.*, vol. 26, no. 7, pp. 1-5, Oct., 2016.
[23] L. Wu, R. Qu, D. Li, and Y. Gao, "Influence of pole ratio and winding pole numbers on performance and optimal design parameters of surface permanent-magnet vernier machines," *IEEE Trans. Ind. Appli.*, vol. 51, no.5, pp. 3707-3715, 2015.
[24] K. Atallah, S. Calverley, and D. Howe, "Design, analysis and realization of a high-performance magnetic gear," *IEE Proc. Electric Power Appl.*, vol. 151, no. 2, pp. 135-143, Mar. 2004.

Yujun Shi received the B.Sc. degree from Hubei Polytechnic University, Huangshi, China, in 2010, and the M.Sc. degree from Jiangsu University, Zhenjiang, China, in 2013.

From 2013 to 2014, he worked as a research assistant in Shenzhen Institutes of Advanced Technology, Chinese Academy of Sciences, Shenzhen, China. He is currently a research assistant with Department of Electrical and Electronic Engineering, Southern University of Science and Technology, Shenzhen, China. His research interests include design, analysis and optimization of permanent-magnet electric machines.

Jin Wei received the B.Sc. degree and the M.Sc. degree from Hefei University of Technology, Hefei, China, in 2009 and 2012, respectively.

From 2012 to 2014, he worked as a research assistant in Shenzhen Institutes of Advanced Technology, Chinese Academy of Sciences, Shenzhen, China. He is currently a research assistant with Department of Electrical and Electronic Engineering, Southern University of Science and Technology, Shenzhen, China. His research interests mainly include mechanical design and manufacturing of permanent-magnet electric machines.

Linni Jian received the B.Eng. degree from Huazhong University of Science and Technology, Wuhan, China, in 2003, the M.Eng. degree from the Institute of Electrical Engineering, Chinese Academy of Sciences, Beijing, China, in 2006, and the Ph.D. degree from The University of Hong Kong, Pokfulam, Hong Kong, in 2010.

He is currently an Assistant Professor in the Department of Electrical and Electronic Engineering, Southern University of Science and Technology, Shenzhen, China. His research interests include the areas of electric drives, power electronics, and smart grids. In these areas, he has published more than 60 referred technical papers, one monograph, and several book chapters. He is also the holder of more than 20 patents.